Article

Comparative assessment of energy-mapping approaches in CT-based attenuation correction for PET.

AY, Mohammad Reza, *et al*.

Abstract

Reliable quantification in positron emission tomography (PET) requires accurate attenuation correction of emission data, which in turn entails accurate determination of the attenuation map (μ-map) of the object under study. One of the main steps involved in CT-based attenuation correction (CTAC) is energy-mapping, or the conversion of linear attenuation coefficients (μ) calculated at the effective CT energy to those corresponding to 511 keV.

Reference

UNIVERSITÉ
DE GENÈVE

MOLECULAR IMAGING AND BIOLOGY

RESEARCH ARTICLE

Comparative Assessment of Energy-Mapping Approaches in CT-Based Attenuation Correction for PET

Mohammad R. Ay,[1,2,3] Maryam Shirmohammad,[1,2] Saeed Sarkar,[1,2] Arman Rahmim,[4] Habib Zaidi[5,6]

[1]Department of Medical Physics and Biomedical Engineering, Tehran University of Medical Sciences, Tehran, Iran
[2]Research Center for Science and Technology in Medicine, Tehran University of Medical Sciences, Tehran, Iran
[3]Research Institute for Nuclear Medicine, Tehran University of Medical Sciences, Tehran, Iran
[4]Department of Radiology, School of Medicine, Johns Hopkins University, Baltimore, MD 21287, USA
[5]Division of Nuclear Medicine, Geneva University Hospital, CH-1211, Geneva 4, Switzerland
[6]Geneva Neuroscience Center, Geneva University, CH-1205, Geneva, Switzerland

Abstract

Introduction: Reliable quantification in positron emission tomography (PET) requires accurate attenuation correction of emission data, which in turn entails accurate determination of the attenuation map (μ-map) of the object under study. One of the main steps involved in CT-based attenuation correction (CTAC) is energy-mapping, or the conversion of linear attenuation coefficients (μ) calculated at the effective CT energy to those corresponding to 511 keV.

Materials and methods: The aim of this study is to compare different energy-mapping techniques including scaling, segmentation, the hybrid method, the bilinear calibration curve technique and the dual-energy approach to generate the μ-maps required for attenuation correction. In addition, our newly proposed method involving a quadratic polynomial calibration curve was also assessed. The μ-maps generated for both phantom and clinical studies were assessed qualitatively and quantitatively. A cylindrical polyethylene phantom containing different concentrations of K_2HPO_4 in water was scanned and the μ-maps calculated from the corresponding CT images using the above-referenced energy-mapping methods. The CT images of five whole-body data sets acquired on a GE Discovery LS PET/CT scanner were employed to generate μ-maps using different energy-mapping approaches that were compared with the μ-maps generated at 511 keV using $^{68}Ge/^{68}Ga$ rod sources. In another experiment, the evaluation was performed on PET images of a clinical study corrected for attenuation using μ-maps generated using the above described methods. The evaluation was performed for three different tissue types, namely, soft tissue, lung, and bone.

Results and Discussion: All energy-mapping methods yielded almost similar results for soft tissues. The mean relative differences between scaling, segmentation, hybrid, bilinear, and quadratic polynomial calibration curve methods and the transmission scan serving as reference were 6.60%, 6.56%, 6.60%, 5.96%, and 7.36%, respectively. However, the scaling method produced the largest difference (16%) for bone tissues. For lung tissues, the segmentation method produced the largest difference (14.9%). The results for reconstructed PET images

Correspondence to: Mohammad R. Ay; *e-mail:* mohammadreza_ay@tums.ac.ir

followed a similar trend. For soft tissues, all energy-mapping methods yield results in nearly the same range. However, in bone tissues, the scaling method resulted in considerable bias in the µ-maps and the reconstructed PET images. The segmentation method also produced noticeable bias especially in regions with variable densities such as the lung, since a single µ is assigned to the lungs. Apart from the aforementioned case, despite small differences in the generated µ-maps, the use of different energy-mapping methods does not affect, to a visible or measurable extent, the reconstructed PET images.

Key words: PET/CT, Attenuation correction, Attenuation map, Energy mapping, Quantification

Introduction

The primary purpose of clinical PET imaging is to visualize and quantify disease-specific radiotracer bio-distributions in the patient's body. There are several parameters that affect the quality and quantitative accuracy of PET images, including positron range [1], the limited spatial resolution and resulting partial volume effect [2], contribution from scattered photons [3], photon attenuation [4], patient motion [5], and the image reconstruction algorithm [6]. Attenuation of photons *in vivo* degrades the visual quality and quantitative accuracy of PET images, thereby adversely affecting interpretation and quantitation of activity concentration. Accurate attenuation correction is therefore mandatory in quantitative PET image reconstruction and plays a pivotal role in clinical PET scanning protocols [7].

In stand-alone PET systems, attenuation correction is usually performed using either rod positron-emitting (^{68}Ga/^{68}Ge) or point single-photon emitting (^{137}Cs) sources orbiting around the patient [8]. Since the energy of photons emitted from positron-emitting rod sources is the same and the γ-rays emitted by ^{137}Cs (662 keV) are very close to the energy of annihilation photons in PET (511 keV), transmission scanning-based attenuation correction is the method of choice for stand-alone PET scanners. In recent years, PET/CT scanners have gained widespread acceptance in the clinical setting since the availability of correlated functional and anatomical images was shown to improve the detection or staging of disease by highlighting areas of increased radiotracer uptake on the anatomical images, whereas regions that look abnormal in the anatomical image can draw attention to a potential area of disease where radio-pharmaceutical uptake may be low. In PET/CT systems, attenuation correction is achieved by X-ray transmission scanning using the CT sub-system of the combined unit [9]. CT-based attenuation correction (CTAC) reduces substantially total scanning time and yields much lower statistical noise in the generated attenuation map (µ-map) even when using low-dose CT scanning protocols [10]. It also eliminates the need for rotating radionuclide transmission sources around the patient but suffers from many drawbacks, including the much higher radiation dose delivered to the patient compared to transmission scanning and the possibility

of producing artifacts in the attenuation corrected PET images [9], particularly in the presence of contrast agent [11–13] and metallic objects in CT images [14, 15].

CT images display the distribution of attenuation coefficients within the patient's body at an effective energy (~55–80 keV) related to the generated X-ray spectra (80–140 kVp). Since the energy of the photons for the emission scan is 511 keV, reliable conversion methods are required to convert the attenuation coefficients (in Hounsfield units) acquired at the CT effective energy to linear attenuation coefficients (µ) at 511 keV. Another important issue is that CT uses a polychromatic X-ray spectrum whereas annihilation photons' energy in PET is monochromatic (511 keV) [16]. Hence, a conversion of the broad energy spectrum attenuation coefficients to linear attenuation coefficients at 511 keV is mandatory.

Several strategies for energy-mapping have been proposed in the literature to map a CT image to a µ-map at 511 keV. These include scaling [17], segmentation [8], hybrid (segmentation/scaling) [9], bilinear calibration curve [16, 18], dual-energy decomposition methods [19, 20], and quadratic polynomial calibration mapping [21]. The latter was recently proposed by our group and assessed using clinical studies. Each of the above-referenced energy-mapping techniques has advantages and drawbacks and, to the best of our knowledge, a comprehensive comparative assessment of these methods has not been performed yet in a clinical setting. Published reports to date compared only two or at most three methods [8, 9, 17]. In our previous study, we reported on the comparative assessment of a number of energy-mapping methods using a small sample of clinical datasets where the evaluation was limited to the generated µ-maps only without assessing the impact on the resulting PET images [22].

The limited number of publications assessing the performance of different energy-mapping methods on the accuracy of the generated µ-maps in CTAC and its impact on the reconstructed PET images spurred the research presented in this work. The aim of this study is to compare the accuracy of different energy-mapping methods through evaluation of generated µ-maps and reconstructed PET images using both experimental phantom and clinical studies. It should be emphasized that although some methods such as scaling and segmentation are less frequently used in

current PET/CT systems, they were considered in our study for complete assessment of different energy-mapping methods proposed so far.

Materials and Methods

Energy-Mapping Approaches

Various energy-mapping strategies were proposed to generate μ-maps at 511 keV from CT images for use in CTAC. These techniques aim to achieve the most accurate conversion possible based on some *a priori* knowledge as described below.

Scaling The scaling method assumes that the ratio of linear attenuation coefficients of any biological tissue is constant for all energies. Hence, the μ-map at 511 keV is produced by multiplying the CT image by the ratio of μ of water at the effective CT and PET photon energies, respectively [9].

Segmentation In this method, the μ-map at 511 keV is generated by segmenting the CT image into different regions corresponding to organs/tissues having different attenuation properties. Then, the CT numbers of each region are replaced with their corresponding μ at 511 keV. It should be noted that two threshold-based segmentation approaches were used. In the first method, referred to as conventional segmentation, the tissues are divided into three classes, namely, soft ($0 \leq HU < 300$), lung ($-800 \leq HU < 0$), and bone ($HU \geq 300$) tissues [9]. Since adipose tissues usually have negative CT numbers, they may be categorized either as soft tissue or lung depending on the thresholds used for segmentation, which might bias the generated μ-map. To reduce this bias, a second segmentation technique (modified segmentation) was developed where an additional class was included for adipose tissue ($-200 \leq HU < 0$). In this case, the range of CT numbers assigned to lung tissue was modified ($-800 \leq HU < -200$).

Hybrid (segmentation/scaling) The hybrid method combines the above described techniques and, as such, the μ-map at 511 keV is formed first by setting a threshold to segment bone from the CT images. This is followed by applying specific scaling factors for bone and non-bone regions. The motivation behind is that the ratio of linear attenuation coefficients for all energies is almost constant for most materials and biological tissues except bone [9].

Bilinear calibration curve In this method, a bilinear calibration curve is obtained by correlating measured CT numbers (HU) of three reference points (air, water, and cortical bone) and their theoretical μ counterparts. The bilinear curve has a break point at the point corresponding to water and yields the μ (in per centimeter) of any material against its CT number. The bilinear method is the most commonly used technique on commercial PET/CT scanners [16].

Dual-energy approach A technically and logistically challenging approach consists in acquiring CT images at two different X-ray beam energies (i.e., peak kilovoltages; kVps) and then using them to extract the individual photoelectric and Compton scattering components to form the μ-map. This method exploits the fact that the Compton scattering contribution to the μ decreases linearly with the inverse of energy (E^{-1}) whereas the photoelectric contribution

decreases as function of E^{-3}. The two separate contributions can be scaled independently and combined to form the μ-map at 511 keV. The dual-energy approach allows for accurate attenuation correction in PET/CT imaging in the presence of high-Z materials, including bone, contrast agents, and metallic objects [19, 20]. The technique seems promising; particularly with the development of dual-source X-ray CT scanners [23] and the introduction of effective CT dose reduction techniques [24, 25].

Quadratic polynomial calibration curve This new method was named as such because it was observed that a quadratic polynomial function best describes the behavior of the calibration curve [22]. This method uses 32 reference points to generate the calibration curve instead of three reference points required by the bilinear curve method. Two of these points represent water and air whereas the remaining 30 points represent samples containing different concentrations of K_2HPO_4 in water from 10 to 1,800 mg/cc. A CT scan was acquired for a cylindrical phantom containing the 30 solutions. The CT numbers of the solutions were obtained from regions of interest (ROIs) delineated on their CT images and their corresponding μ at 511 keV were computed using the XCOM photon cross-section library [26]. The μ of each material was subsequently plotted against its CT number. For HU<0 the plotted curve was similar to the conventional bilinear curve. However, for HU≥0, a quadratic polynomial function was fitted to the points with 95% confidence band. A typical calibration curve generated at 140 kVp is shown in Fig. 1 along with the conventional bilinear calibration curve.

CT and PET/CT Scanners

The 64-slice Light Speed VCT scanner (GE Healthcare Technologies, Waukesha, WI) equipped with Highlight ($Y_2Gd_2O_3$:Eu) ceramic scintillators was used in phantom studies. This third generation CT scanner has a 540-mm source-to-isocenter and 950-mm source-to-detector distances, 58,368 individual detector elements arranged in 64 rows of 0.625 mm thickness at isocenter, each containing 888 active patient elements and 24 reference elements. The scanner is equipped with the Performix Pro anode grounded metal-ceramic tube unit which uses 56° fan angle, 7° target angle and minimum inherent filtration of 3.25 mm Al and 0.1 mm Cu at 140 kVp.

The Discovery LS (DLS) PET/CT scanner (GE Healthcare Technologies, Waukesha, WI) was used for comparison of μ-maps derived from CT and those obtained using the transmission-based approach using $^{68}Ge/^{68}Ga$ rod sources. The DLS scanner has the capability of producing both transmission-based and CT-based μ-maps. The scanner uses BGO crystals of dimensions $4 \times 8 \times 30$ mm^3 in the tangential, axial and radial directions, respectively. The detector blocks are arranged into 18 rings and 672 crystals per ring. The system allows for simultaneous acquisition of 35 transaxial slices.

The Discovery RX (DRX) PET/CT scanner (GE Healthcare Technologies, Waukesha, WI) was used to assess the impact of various energy-mapping techniques on reconstructed PET data. The scanner uses LYSO crystals arranged in the form of 24 rings and 630 crystals per ring. The LYSO crystals ($4.2 \times 6.3 \times 30$ mm^3) are arranged into 9×6 blocks. It should be noted that recent software implemented on both DLS and DRX scanners use the tri-linear calibration curve method for energy-mapping where a different scale is used for each of the kVp settings (80, 100, 120 and 140 kVp) to account for the change in bone HU with kVp.
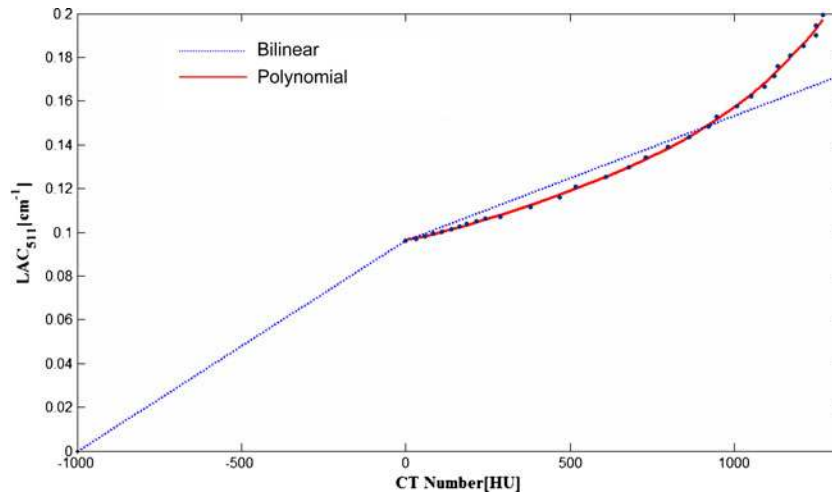
Fig. 1. Plots showing the conventional bilinear calibration curve (*dotted line*) compared to the quadratic polynomial calibration curve (*solid line*).

Phantom Studies

A polyethylene cylindrical phantom (250 ± 0.5 mm diameter) was constructed to assess the accuracy of μ-maps generated using the above described energy-mapping methods. This phantom consisted of 16 cylindrical holes (20 ± 0.5 mm diameter) with four holes in the middle (5 ± 0.5 mm diameter) filled with air. One of the 16 holes was filled with water and the rest with various concentrations of K_2HPO_4 in water from 60 to 1,800 mg/cc (μ ranging from 0.1 to 0.2 cm^{-1} at 511 keV) to simulate different biological tissues. It should be noted that K_2HPO_4 solutions having concentrations ranging between 800 and 1,800 mg/cc simulate bone with different densities in the human body.

This phantom was scanned on the LightSpeed VCT scanner dedicated to cardiac imaging using a tube voltage of 120 kVp and current of 400 mA with a 1-s rotation speed. The acquired CT images were converted to μ-maps using the various energy-mapping methods. The theoretical μ at 511 keV for each concentration of the K_2HPO_4 solution was computed using the XCOM photon cross-section library [26], and served as reference standard for assessment of the phantom studies. It should be noted that the quadratic polynomial calibration curve method was not evaluated here since the same phantom and experimental setup were used to extract the fitting parameters. For the dual-energy method, different combinations of kVps were utilized to find the optimum combination of tube voltages used in this technique.

Clinical Studies

Five CT images selected from the clinical database of whole-body PET/CT scans were used for the assessment of various energy-mapping methods in a clinical setting. The data were acquired on a GE Discovery LS PET/CT scanner. The corresponding μ-maps were created by converting the acquired CT images using the above-referenced energy-mapping approaches. Note that the dual-energy technique was not performed on the clinical studies since the CT data were acquired using a single kVp setting given that the additional dose to the patient resulting from a second CT scan was not justified in this context. Transmission images acquired using $^{68}Ge/^{68}Ga$ rod sources following the CT scan served as reference

standard for assessment of the various energy-mapping techniques. Following hardware failure on the scanner, it was not possible to retrieve the corresponding PET raw data for further analysis.

Further assessment of the impact of various energy-mapping techniques on reconstructed PET images was carried out using a patient PET/CT data set. The data were acquired on a GE Discovery RX PET/CT scanner. Similar to the methodology followed for the previous studies, the CT images of the patient were converted to μ-maps and used to attenuation correct the PET data for photon attenuation. The obtained PET images were then assessed through comparison with those attenuation corrected using the μ-map generated by software provided by the manufacturer used as reference. This was deemed a reasonable approach in the absence of a reference standard providing the ground truth for objective performance assessment of clinical data.

Attenuation Correction and Image Reconstruction

The CT-based μ-maps at 511 keV were generated as follows: the CT image matrix size (512×512) was first down sampled to match the PET image matrix size (128×128) followed by energy-mapping using the techniques described earlier. The last step consisted of Gaussian smoothing to match the resolution of PET images. The full-width at half-maximum (FWHM) of the Gaussian filter was set to 5 mm for phantom studies. For the DLS and DRX clinical studies, different FWHMs were tested to find the optimal width of the Gaussian filter that resulted in the closest match to the resolution of the scanner-generated μ-maps. Therefore, a FWHM of 8 and 12 mm were set for DLS and DRX CT images, respectively. The PET reconstruction technique described in [27] was used to reconstruct the clinical data set. A post-reconstruction 3D Gaussian smoothing filter with a kernel of 4.18 mm as used in the clinic for whole-body PET studies was applied.

Assessment Strategy

A region-of-interest (ROI)-based quantitative analysis was performed on phantom and clinical studies for the assessment of

various energy-mapping strategies. Several ROIs were defined on regions of the μ-map corresponding to different concentrations of the K_2HPO_4 solutions and the mean μ was computed. The result was then compared to the theoretical μ estimated using the XCOM photon cross-section library [26]. The assessment was performed on two sets corresponding to regions with low concentration (≤180 mg/cc) of K_2HPO_4, representing soft tissue, and regions with high concentration (>180 mg/cc) of K_2HPO_4 representing high density tissues.

For quantitative assessment of patients' μ-maps, ROIs with different size were delineated in various anatomical regions. Since the μ-maps were derived from a single CT image, all the ROIs were exactly in the same position. Likewise, the ROIs were also defined in the same regions on the transmission maps taking into account slight patient movement between CT and transmission scans when appropriate. Overall, 455 ROIs were defined on the five clinical CT images comprising 223 ROIs delineated on soft tissues, 163 ROIs on bone structures and 69 ROIs on the lungs. The μ for each ROI on the generated μ-maps was then compared to the μ of the reference ROI defined on the transmission map. The magnitude of the mean relative difference between the CT- and transmission-based results for each group was considered as figure of merit for assessment of the different methods.

Similarly, different ROIs were defined on the reconstructed PET images corrected using the various energy-mapping approaches and the one corrected using the μ-map generated by the software provided by the vendor. A total of 215 ROIs were defined consisting of 143 ROIs on soft tissues, 41 ROIs on the lungs and 31 ROIs on bone tissues. The ROIs defined for quantitative analysis were carefully selected to encompass various anatomical regions except the bladder. The magnitude of the mean relative difference and the correlation coefficient between results obtained when using each method and the one serving as reference for comparison, were computed. The relative difference between PET images corrected using the different μ-maps and reference PET images were compared and the results summarized in the form of box-and-whisker plots.

Results

Phantom Studies

As mentioned earlier, several combinations of tube voltages during the implementation of the dual-energy method were carried out to find the optimum combination. Since the VCT CT scanner has four operational kVps (80, 100, 120, and 140 kVp), six different combinations were used and the generated μ-maps compared with the theoretical estimates calculated using XCOM. Fig. 2 illustrates the phantom μ-maps generated using the dual-energy method implemented in the image domain for different combinations of X-ray tube voltages. Table 1 summarizes the mean relative difference between the measured and theoretical attenuation coefficients for each combination of kVps. It appears that tube voltages of 80 and 140 kVp produce the smallest relative error compared to other combinations. The relative contribution of photoelectric and Compton scattering cross-sections to the total μ can be characterized more accurately when using two energies (kVp) producing maximum difference. This combination was selected for further assessment of the different techniques.

Table 2 summarizes the mean relative difference between the measured and theoretical attenuation coefficients for the various samples when using different energy-mapping methods. The results presented were averaged for low and
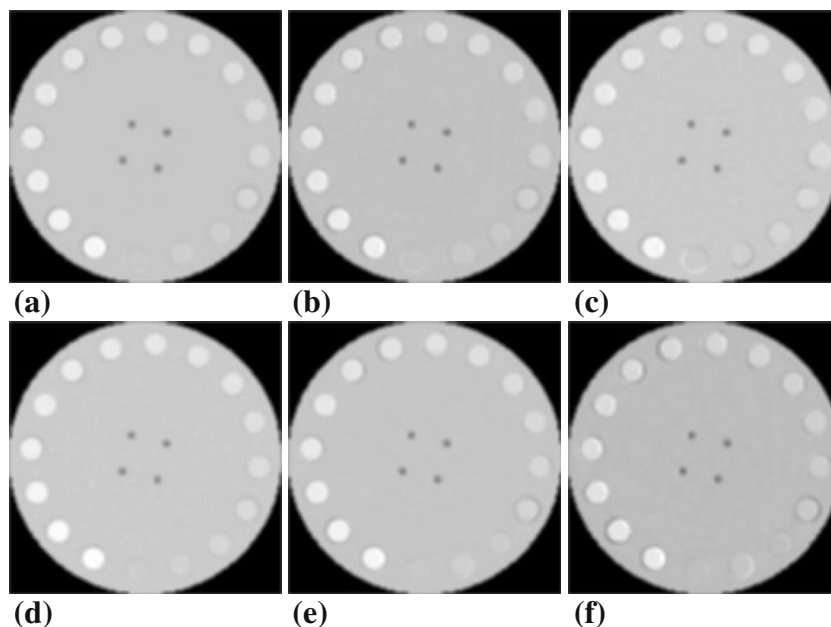

Fig. 2. Attenuation maps of the phantom generated using the dual-energy approach with different combinations of X-ray tube voltages: 80–100 kVp (**a**), 80–120 kVp (**b**), 80–140 kVp (**c**), 100–120 kVp (**d**), 100–140 kVp (**e**), and 120–140 kVp (**f**).

Table 1. Mean relative difference (in %) between the attenuation coefficients derived using the dual-energy method for different combinations of kVps and the theoretical linear attenuation coefficients calculated using the XCOM photon cross-section library for various regions corresponding to different concentrations of K_2HPO_4

Material	CT Number at 120 kVp (HU)	μ at 511 keV [cm^{-1}]	80–100 kVp	80–120 kVp	80–140 kVp	100–120 kVp	100–140 kVp	120–140 kVp
Air	−1,000	0	0.00	0.00	0.00	0.00	0.00	0.00
H_2O	0	0.096	0.21	0.94	0.11	0.42	0.73	0.42
0.12[a]	163	0.102	0.39	2.53	2.14	4.48	3.12	2.34
0.18	240	0.106	3.30	2.54	2.26	7.63	2.83	1.23
0.24	375	0.109	3.01	3.65	4.47	4.20	3.56	4.11
0.30	420	0.112	3.90	3.72	4.17	3.63	4.17	4.08
0.36	486	0.116	3.19	4.48	4.65	5.25	4.57	4.39
0.48	608	0.123	1.87	3.17	3.82	4.07	3.58	3.41
0.54	668	0.126	1.87	1.90	2.69	2.53	2.69	2.13
0.60	678	0.129	1.15	1.16	2.62	2.47	2.31	1.77
0.66	730	0.133	1.38	1.98	2.55	1.65	2.25	1.28
0.72	770	0.136	1.24	1.66	0.88	1.02	1.10	1.59
0.84	861	0.143	2.99	1.74	0.63	0.21	0.63	1.53
0.90	918	0.147	4.55	3.13	2.17	0.88	1.83	2.58
1.20	1060	0.164	11.14	9.01	6.82	6.57	6.82	7.85
1.50	1160	0.181	16.34	14.25	12.32	12.76	12.87	13.75
1.80	1270	0.199	21.02	19.17	17.61	17.26	17.66	18.51
Mean±SD	–	0.12±0.0	4.56±5.9	4.41±5.1	4.11±4.6	4.41±4.6	4.16±4.6	4.17±4.9

[a]Concentration (in grams per cubic centimeter) of K_2HPO_4 in water

high concentrations of K_2HPO_4 to allow modeling of soft tissue and bony structures (Fig. 3). For low concentrations of K_2HPO_4, the mean relative difference between theoretical and calculated attenuation coefficients when using scaling, segmentation, hybrid, bilinear, and dual-energy methods are 9.3%, 3.1%, 3.0%, 4.5%, and 1.3%, respectively. They are 31.4%, 19.9%, 11.7%, 11.0%, and 5.1%, respectively, for high concentrations of K_2HPO_4. Therefore, all energy-mapping techniques yield average differences lower than 10% for low concentrations of K_2HPO_4. However, for higher concentrations of K_2HPO_4, the scaling and segmentation methods result in relatively high relative differences compared to other methods. The original CT image and μ-maps

of the phantom generated using various energy-mapping techniques are shown in Fig. 4.

Clinical Studies

Fig. 5 shows typical μ-maps generated using the different energy-mapping techniques together with the transmission-based μ-map for one clinical study. As described earlier, the ROIs defined on the patients' μ-map were segmented into soft, lung, and bone tissues. Fig. 6 shows the mean relative difference between μ-maps generated using the different energy-mapping methods and the transmission method used as reference. The paired t test statistical analysis did not

Table 2. Mean relative difference (in %) between the attenuation coefficients obtained when using various energy-mapping techniques and the theoretical linear attenuation coefficients computed using the XCOM photon cross-section library for different regions within the phantom

Material	μ at 511 keV [cm^{-1}]	Scaling	Segmentation	Hybrid	Bilinear	Dual-energy
Air	0	0	0	0	0	0
H_2O	0.096	0.00	0.00	0.00	0.00	0.42
0.12[a]	0.102	9.84	6.43	8.87	4.48	2.34
0.18	0.106	18.00	2.73	0.09	9.14	1.23
0.24	0.109	22.47	0.46	3.65	9.95	4.11
0.30	0.112	25.44	3.37	6.21	11.35	4.08
0.36	0.116	28.60	6.12	8.79	11.71	4.39
0.48	0.123	32.44	11.38	12.20	13.41	3.41
0.54	0.126	32.49	13.83	12.41	13.28	2.13
0.60	0.129	34.28	16.02	14.02	13.56	1.77
0.66	0.133	36.08	18.23	15.98	14.55	1.28
0.72	0.136	37.09	20.26	16.53	14.56	0.59
0.84	0.143	37.19	24.09	15.60	13.02	1.53
0.90	0.147	36.14	25.95	16.30	12.64	2.58
1.20	0.164	34.08	33.66	14.85	9.07	7.85
1.50	0.181	28.05	40.04	10.07	3.47	13.75
1.80	0.199	23.83	45.31	6.07	2.66	18.51
Average±SD	0.12±0.0	25.65±12.2	15.76±14.2	9.51±6.0	9.23±5.1	4.12±5.0

[a]Concentration (in grams per cubic centimeter) of K_2HPO_4 in water
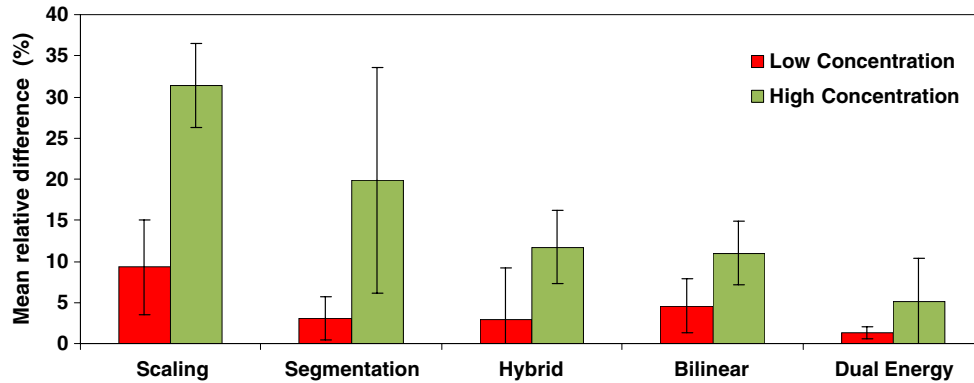
Fig. 3. Mean relative difference of linear attenuation coefficients (μ) calculated using different energy-mapping methods for low (≤180 mg/cc) and high (>180 mg/cc) concentrations of K_2HPO_4 solution modeling soft tissue and bony structures, respectively.

reveal statistically significant differences among the various μ-maps derived from CT and those obtained using the transmission-based approach. For soft tissues, the mean relative differences for the scaling, conventional segmentation, modified segmentation, hybrid, bilinear, and quadratic polynomial calibration curve methods are 6.6%, 6.6%, 6.4%, 6.6%, 6.0%, and 7.4%, respectively, which are indeed quite similar. For lung, they are 8.4%, 14.9%, 14.9%, 8.4%, 8.4%, and 8.4%, respectively. Therefore, for lung tissues, segmentation techniques produce relatively higher relative differences compared to other methods. However, for bone tissues, the mean relative differences for the aforementioned methods are 16.0%, 5.7%, 5.7%, 6.8%, 6.8%, and 6.8%, respectively. Consequently, the scaling method yields the highest relative difference and as such special caution is required in bony structures when using this method. The remaining energy-mapping methods yield very similar results.

Taking the analysis one step further, the impact of different energy-mapping methods was assessed on attenuation corrected clinical whole-body FDG-PET data. In the absence of a true reference standard, the various AC-corrected PET images were compared to those attenuation corrected using the μ-map produced by the vendor-supplied software as a reference. Fig. 7 shows coronal PET slices corrected for attenuation using the different μ-maps whereas Fig. 8 shows difference images obtained by subtracting PET images corrected for attenuation using the different energy-mapping techniques and the reference image in sagittal view. The motivation behind the choice of the sagittal plane is to focus on the spine as a large bony structure. However, other tissues such as soft tissue and lungs are also visible in this view.

It should be emphasized that the dark regions correspond to areas of overestimation and light regions areas of underestimation of activity concentrations (i.e., over-correc-
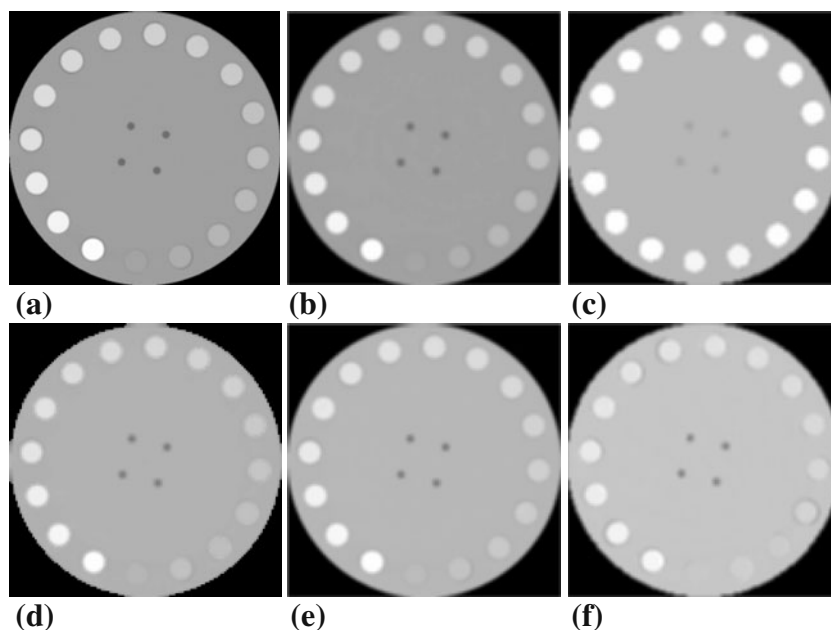

Fig. 4. Original CT image (**a**) and generated attenuation maps using different energy-mapping methods assessed in this work: scaling (**b**), segmentation (**c**), hybrid (**d**), bilinear (**e**) and dual-energy (80 and 140 kVp) (**f**).
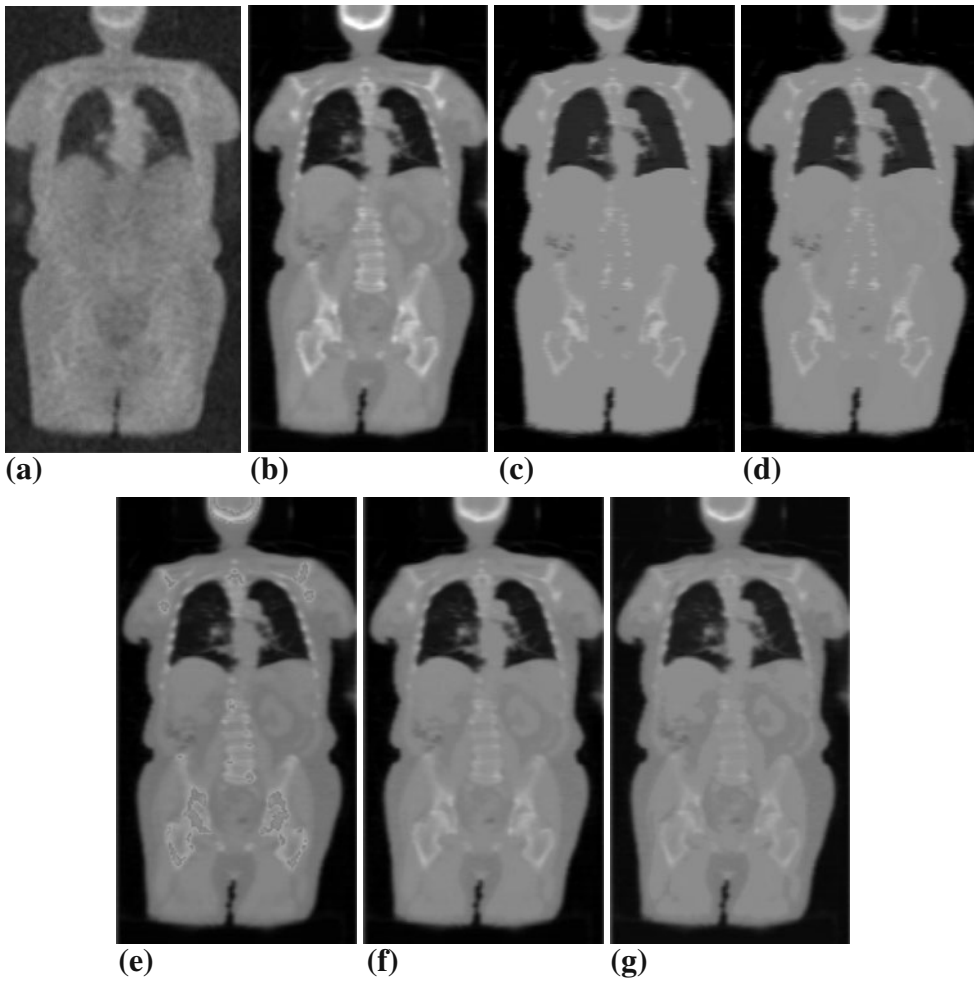
Fig. 5. Illustration of attenuation maps generated using the different energy-mapping techniques: (**a**) transmission scanning, (**b**) scaling, (**c**) conventional segmentation, (**d**) modified segmentation, (**e**) hybrid, (**f**) bilinear, and (**g**) quadratic polynomial curve methods.

tion and under-correction for attenuation, respectively) compared to the reference PET images. For example, in the difference image between the PET image corrected using the scaling method and the reference PET image (Fig. 8a), bone appears dark, indicating that the scaling method over-corrects for attenuation and thus overestimates the activity concentrations in bony regions. Conversely, in the difference

image between the PET image corrected using the bilinear method and the reference PET image (Fig. 8e), most areas are light, indicating that the bilinear method under-corrects for attenuation and as such underestimates the activity concentrations. However, the difference image is actually quite faint overall and thus indicates that the attenuation correction and the estimates of activity concentrations are
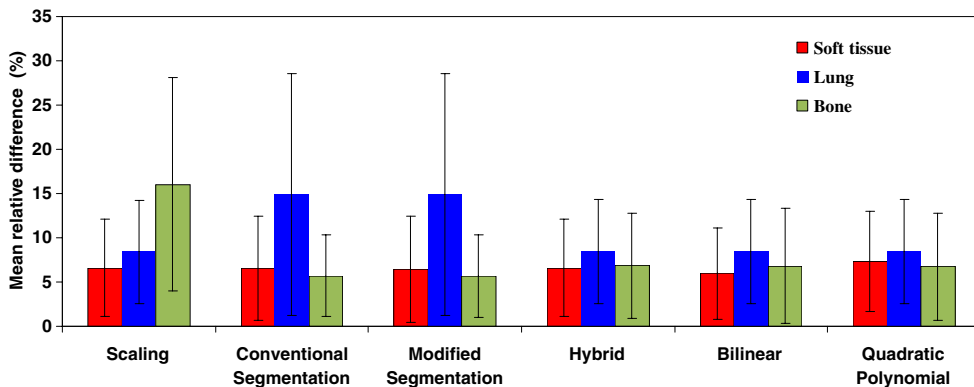

Fig. 6. Mean relative difference between attenuation maps generated using the different energy-mapping techniques and the one generated using transmission scanning for different tissue types.
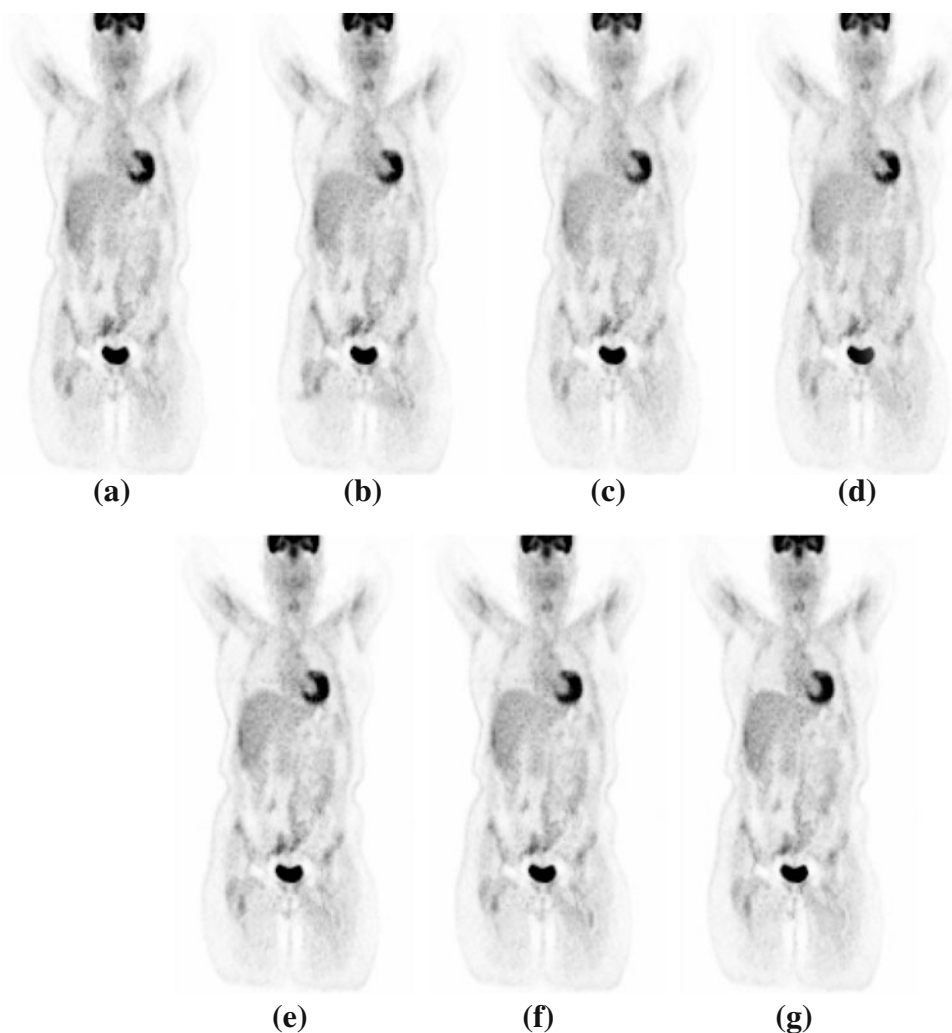
Fig. 7. Representative coronal slices of PET images corrected for attenuation using attenuation maps obtained through different energy-mapping techniques: (**a**) PET image corrected using the μ-map generated by the software supplied by the vendor; (**b**) scaling method; (**c**) conventional segmentation; (**d**) modified segmentation; (**e**) hybrid; (**f**) bilinear; and (**g**) quadratic polynomial calibration curve methods.

fairly accurate. This is expected, since the reference PET images were corrected for attenuation using μ-maps generated with the vendor-supplied software, and this also employs a bilinear algorithm [18].

Fig. 9 shows a box-and-whisker plot of the mean relative difference between PET images corrected for attenuation using the different μ-maps and the reference PET image for soft tissue, lung, and bone. For soft tissues, the mean relative difference obtained for both segmentation approaches are higher (7.9% for conventional segmentation and 7.2% for modified segmentation) than the other methods. Likewise, segmentation methods produce the highest mean relative differences for lung tissue (11.3% for conventional segmentation and 11.0% for modified segmentation). For bone, the scaling method yielded the largest deviation (9.5%) whereas the bilinear and quadratic polynomial calibration curve methods yielded the lowest mean relative difference (1.7% and 1.3%, respectively).

In the box-and-whisker plot, the top and bottom of each box represent the 25th and 75th percentiles of the samples' estimate, respectively. The distance between the top and bottom represent the inter-quartile ranges. The line in the middle of each box represents the sample median. When the median line is almost centered in the box, the samples are equally distributed. The whiskers are lines extending above and below each box. Whiskers are drawn from the end of the inter-quartile range to the furthest observations within the whisker length by default. The most extreme values are within 1.5 times the inter-quartile range from the end of the box. Observations beyond the whisker length are marked as outliers. An outlier is an estimate that is more than 1.5 times the inter-quartile range away from the top or bottom of the box. Outliers are displayed with a red plus sign. When the upper quartile of a box is higher for one technique in a given region (the length of the box is bigger), it is an indication that the method is not precise for that region. For example,
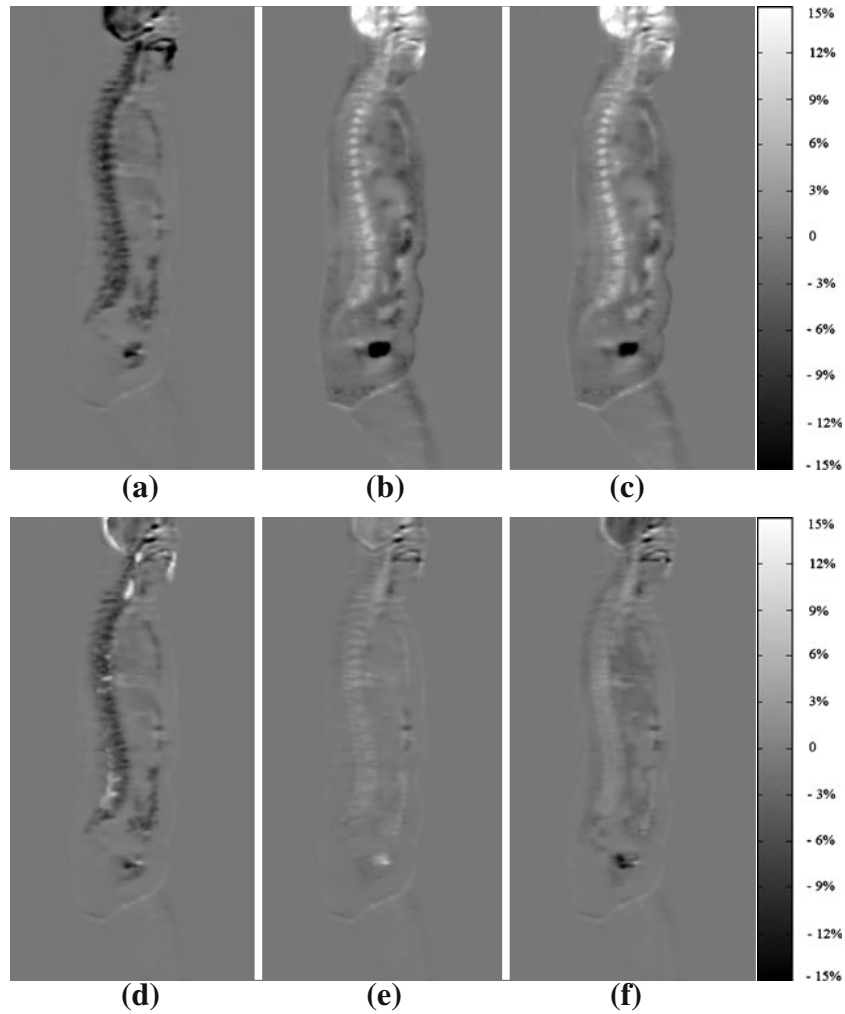
Fig. 8. Representative difference between PET images shown in Fig. 7 corrected using the µ-map generated by the software supplied by the vendor and those corrected for attenuation using scaling (**a**); conventional segmentation (**b**); modified segmentation (**c**); hybrid (**d**); bilinear (**e**) and quadratic polynomial calibration curve (**f**) methods.
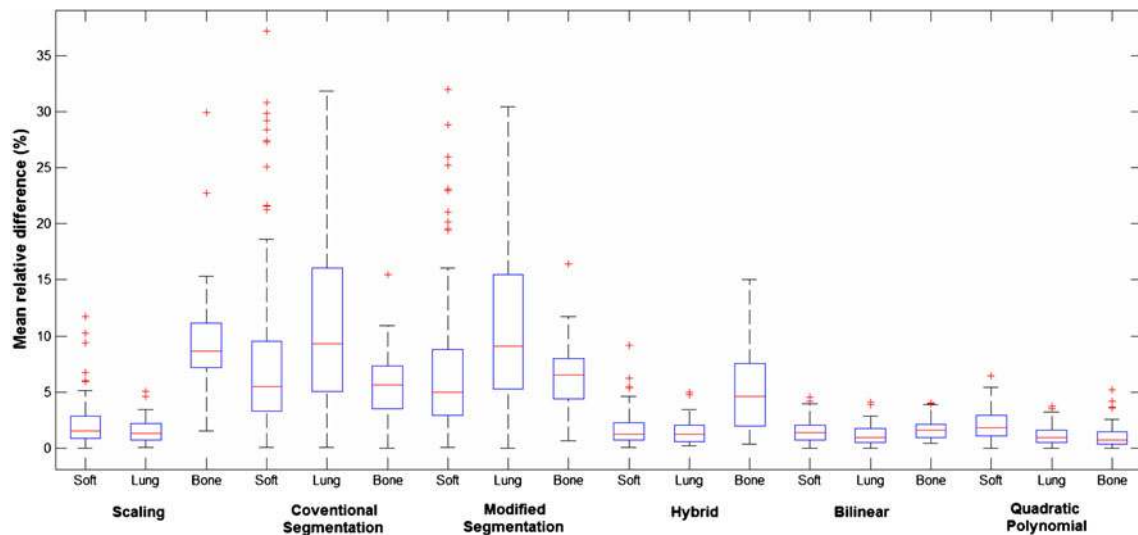

Fig. 9. Box-and-whisker plot of the mean relative difference between PET images corrected for attenuation using attenuation maps generated using the different energy-mapping techniques and the one corrected using the µ-map generated by the software supplied by the manufacturer (the *top* and *bottom* of each box represent the 25th and 75th percentiles of the samples' estimates, respectively).

the scaling method was found to produce noticeable error for bone regions. Likewise, the segmentation technique was found to result in large deviations in the lungs. Consequently, their corresponding boxes are longer than the other boxes. Therefore, the scaling and segmentation methods result in inaccurate estimates for bone regions and lungs, respectively. The length of the whiskers illustrates the spread of mean relative differences. For instance, whiskers of lung tissues for segmentation methods are longer compared to other regions and reflect the dispersion of lung tissue estimates. As far as segmentation-based attenuation correction is concerned, the lung is one of the most challenging organs [8] given that it has been shown that the density of lung tissue is considerably different from subject to subject, depends on breathing patterns and varies by as much as 30% with age and in the presence of pulmonary disease [28].

The correlation coefficient resulting from the ROI-based analysis comparing PET images corrected for attenuation using different energy-mapping methods and the PET image corrected using the μ-map generated by the software supplied by the manufacturer are summarized in Table 3. There is very good agreement between different energy-mapping methods for soft tissues where the correlation coefficients are very close to unity (0.998–0.999). This is in contrast with other regions where lower correlation coefficients were obtained (0.733 and 0.744 for both segmentation techniques when applied to lung tissues and 0.865 for scaling when applied to bone tissues). Overall, the bilinear and quadratic polynomial calibration curve methods have the highest correlation coefficients whereas scaling and segmentation methods yield the lowest correlation coefficients. Similar results were obtained when analyzing the clinical μ-maps.

Discussion

The ability to perform accurate attenuation correction with validated hardware/software algorithms combined with the utilization of rigorous quality control measures enhances the interpretive confidence and accuracy of molecular PET imaging. Consequently, there has been growing acceptance of the need to systematically perform attenuation correction in clinical setting following its successful implementation in research environments [7]. It has been shown using phantom

Table 3. Summary of correlation coefficients resulting from the ROI-based analysis of PET images corrected for attenuation using the various energy-mapping methods and PET images produced using the software supplied by the manufacturer

Energy-mapping method	Soft tissue	Lung	Bone
Scaling	0.999	0.997	0.865
Conventional segmentation	0.998	0.733	0.982
Modified segmentation[a]	0.998	0.744	0.984
Hybrid (segmentation/scaling)	0.999	0.995	0.986
Bilinear calibration curve	0.999	0.996	0.998
Quadratic polynomial calibration curve	0.999	0.996	0.995

[a]See description provided in the "Energy-Mapping Approaches" section

studies that for low concentrations of K_2HPO_4, the relative differences between energy-mapping-derived and theoretical attenuation coefficients are less than 10% (Fig. 4). However, for higher concentrations of K_2HPO_4, both scaling and segmentation methods led to larger deviations in these regions compared to other techniques. The results of the clinical μ-map and PET data analysis are consistent with these observations. Therefore, in soft tissue regions where high atomic number tissues such as bones are absent, all energy-mapping methods yield very similar results and may be used interchangeably for attenuation correction of PET data. The high relative difference reported for the scaling method in bone regions is attributed to the abundance of calcium and phosphor in bone, which has a high photoelectric interaction cross-section. The predominant interaction process at X-ray CT energies (~70 keV) is Compton scattering in soft tissue and photoelectric interaction in bone. However, the predominant interaction process at 511 keV is Compton scattering for both tissue types. For lung tissues, all energy-mapping methods result in acceptable μ-maps except segmentation techniques (Fig. 6). The main drawback of segmentation techniques when applied to regions with variable density, such as lungs [28], is the high inaccuracy that might occur when a threshold is set to discriminate tissues with large CT number variability followed by assignment of a single attenuation coefficient. It was also shown in phantom studies that segmentation methods produce a very large difference (19.9%) compared to the theoretical values in regions with high concentrations of K_2HPO_4 since the CT numbers of all K_2HPO_4 solutions are replaced with a single attenuation coefficient regardless of their density. Segmentation-based MR-guided attenuation correction in PET/MR will therefore likely be problematic as well [29]. The low relative difference for the bilinear method in the region corresponding to a concentration of 1,800 mg/cc reflects the fact that this point was itself used for the derivation of the bilinear calibration curve, thus resulting in minimal subsequent errors (Table 2).

The newly proposed quadratic polynomial calibration curve energy-mapping method yielded relatively good agreement with reference μ-maps for soft tissues, lung and bone tissues. With respect to the analysis of the reconstructed PET images, the differences between different energy-mapping techniques are more pronounced in μ-maps than in reconstructed PET images. This is in agreement with previous studies reporting similar assessment of the impact of the attenuation map on reconstructed PET images [15, 30]. Nevertheless, despite the lower deviations, the results followed the same trend as the μ-maps.

Segmentation methods resulted in mean differences less than 8% for soft and bone tissues and up to 12% for lung tissues (Fig. 8). PET images obtained using the scaling method produce a large difference compared to the reference image in bone regions owing to the high photofraction of bone. The results obtained using the quadratic polynomial calibration curve method when applied to clinical data seem

to be reliable in all tissue types (Figs. 6 and 8). Although our present analysis did not show substantial difference among PET images generated using the different energy-mapping methods for the derivation of the attenuation map, whether or not this results in clinically relevant differences remains an open question which requires further investigation using sufficient clinical data.

Conclusion

Attenuation correction of PET data plays an important role in the interpretation and quantitative analysis of the biodistribution of biologically relevant probes in the human body. In this study, the μ-maps generated using different energy-mapping techniques were compared and their impact on resulting clinical PET/CT images assessed. An interesting outcome of this study is that for attenuation correction of low atomic number tissues such as soft tissues, the different energy-mapping methods yield acceptable μ-maps resulting in comparable attenuation corrected PET images. However for lung and bone tissues, segmentation methods results in significant bias which might affect the accuracy of the obtained results. Likewise, the scaling method overestimates the attenuation coefficients of bone tissues and thus the activity concentration in the corresponding PET images. Further assessment of the robustness of the newly proposed quadratic polynomial calibration curve method is guaranteed. Overall, it can be concluded that despite the differences in the μ-maps generated using different energy-mapping methods, their use for attenuation correction do not affect to a significant extent the reconstructed PET images, except for segmentation and scaling techniques.

References

1. Sanchez-Crespo A, Andreo P, Larsson SA (2004) Positron flight in human tissues and its influence on PET image spatial resolution. Eur J Nucl Med Mol Imaging 31:44–51
2. Rousset O, Rahmim A, Alavi A, Zaidi H (2007) Partial volume correction strategies in PET. PET Clinics 2:235–249
3. Zaidi H, Koral KF (2004) Scatter modelling and compensation in emission tomography. Eur J Nucl Med Mol Imaging 31:761–782
4. Zaidi H, Hasegawa BH (2003) Determination of the attenuation map in emission tomography. J Nucl Med 44:291–315
5. Osman MM, Cohade C, Nakamoto Y, Wahl RL (2003) Respiratory motion artifacts on PET emission images obtained using CT attenuation correction on PET-CT. Eur J Nucl Med Mol Imaging 30:603–606
6. Lartizien C, Kinahan PE, Swensson R, Comtat C, Lin M, Villemagne V, et al (2003) Evaluating image reconstruction methods for tumor detection in 3-dimensional whole-body PET oncology imaging. J Nucl Med 44:276–290
7. Bai C, Kinahan PE, Brasse D, Comtat C, Townsend DW, Meltzer CC, et al (2003) An analytic study of the effects of attenuation on tumor detection in whole-body PET oncology imaging. J Nucl Med 44:1855–1861
8. Kinahan PE, Hasegawa BH, Beyer T (2003) X-ray-based attenuation correction for positron emission tomography/computed tomography scanners. Semin Nucl Med 33:166–179
9. Kinahan PE, Townsend DW, Beyer T, Sashin D (1998) Attenuation correction for a combined 3D PET/CT scanner. Med Phys 25:2046–2053

10. Ay M, Zaidi H (2006) Computed Tomography-based attenuation correction in neurological positron emission tomography: evaluation of the effect of x-ray tube voltage on quantitative analysis. Nucl Med Commun 27:339–346
11. Mawlawi O, Erasmus JJ, Munden RF, Pan T, Knight AE, Macapinlac HA, et al (2006) Quantifying the effect of IV contrast media on integrated PET/CT: clinical evaluation. AJR Am J Roentgenol 186:308–319
12. Ahmadian A, Ay MR, Bidgoli JH, Sarkar S, Zaidi H (2008) Correction of oral contrast artifacts in CT-based attenuation correction of PET images using an automated segmentation algorithm. Eur J Nucl Med Mol Imaging 35:1812–1823
13. Ay M, Zaidi H (2006) Assessment of errors caused by x-ray scatter and use of contrast medium when using CT-based attenuation correction in PET. Eur J Nucl Med Mol Imaging 33:1301–1313
14. DiFilippo FP, Brunken RC (2005) Do implanted pacemaker leads and ICD leads cause metal-related artifact in cardiac PET/CT? J Nucl Med 46:436–443
15. Lemmens C, Montandon M-L, Nuyts J, Ratib O, Dupont P, Zaidi H (2008) Impact of metal artefacts due to EEG electrodes in brain PET/CT imaging. Phys Med Biol 53:4417–4429
16. Bai C, Shao L, Da Silva A, Zhao Z (2003) A generalized model for the conversion from CT numbers to linear attenuation coefficients. IEEE Trans Nucl Sci 50:1510–1515
17. Beyer T, Kinahan PE, Townsend DW, Sashin D (1994) The use of X-ray CT for attenuation correction of PET data. Proc IEEE Nuclear Science Symposium and Medical Imaging Conference. 30 Oct.-5 Nov., Norfolk, VA, USA, 1573–1577
18. Burger C, Goerres G, Schoenes S, Buck A, Lonn AHR, Von Schulthess GK (2002) PET attenuation coefficients from CT images: experimental evaluation of the transformation of CT into PET 511-keV attenuation coefficients. Eur J Nucl Med 29:922–927
19. Guy MJ, Castellano-Smith IA, Flower MA, Flux GD, Ott RJ, Visvikis D (1998) DETECT-dual energy transmission estimation CT-for improved attenuation correction in SPECT and PET. IEEE Trans Nucl Sci 45:1261–1267
20. Kinahan PE, Alessio AM, Fessler JA (2006) Dual energy CT attenuation correction methods for quantitative assessment of response to cancer therapy with PET/CT imaging. Technol Cancer Res Treat 5:319–327
21. Shirmohammad M, Ay M, Sarkar S, Ghadiri H, Rahmim A (2008) Comparative assessment of different energy mapping methods for generation of 511 KeV attenuation map from CT images in PET/CT systems: a phantom study. The Fifth IEEE International Symposium on Biomedical Imaging: From Nano to Macro. Paris, France, pp 644–647
22. Shirmohammad M, Ay M, Rahmim A, Sarkar S, Zaidi H (2008) A novel energy mapping method for attenuation map generation at 511 keV in computed tomography based attenuation correction [abstract]. Eur J Nucl Med Mol Imaging 35:S146
23. Flohr TG, McCollough CH, Bruder H, Petersilka M, Gruber K, Suss C, et al (2006) First performance evaluation of a dual-source CT (DSCT) system. Eur Radiol 16:256–268
24. Greess H, Lutze J, Nomayr A, Wolf H, Hothorn T, Kalender WA, et al (2004) Dose reduction in subsecond multislice spiral CT examination of children by online tube current modulation. Eur Radiol 14:995–999
25. Wang J, Li T, Lu H, Liang Z (2006) Noise reduction for low-dose single-slice helical CT sinograms. IEEE Trans Nucl Sci 53:1230–1237
26. Berger MJ, Hubbell JH, Seltzer SM, Chang J, Coursey JS, Sukumar R, et al (1998) XCOM: photon cross sections database. Report NBSIR 87-3597. Gaithersburg: Ionizing Radiation Division, Physics Laboratory, National Institute of Standards and Technology, Gaithersburg, MD 20899. Available at http://physics.nist.gov/PhysRefData/Xcom/Text/XCOM.html
27. Rahmim A, Tang J, Lodge MA, Lashkari S, Ay MR, Lautamaki R, et al (2008) Analytic system matrix resolution modeling in PET: an application to Rb-82 cardiac imaging. Phys Med Biol 53:5947–5965
28. Robinson PJ, Kreel L (1979) Pulmonary tissue attenuation with computed tomography: comparison of inspiration and expiration scans. J Comput Assist Tomogr 3:740–748
29. Zaidi H (2007) Is MRI-guided attenuation correction a viable option for dual-modality PET/MR imaging? Radiology 244:639–642
30. Nahmias C, Lemmens C, Faul D, Carlson E, Long M, Blodgett T, et al (2008) Does reducing CT artifacts from dental implants influence the PET interpretation in PET/CT studies of oral cancer and head and neck cancer? J Nucl Med 49:1047–1052